Towards Global Stability Analysis of Flexible Aircraft in Edge-of-the-Envelope Flow

Jelle Houtman* and Sebastian Timme†
University of Liverpool, Liverpool, L69 3GH, United Kingdom

Shock buffet on wings is a phenomenon caused by strong shock-wave/boundary-layer interaction resulting first in self-sustained flow unsteadiness and eventually in a detrimental structural response called buffeting. While it is an important aspect of aircraft design and certification, particularly for modern transonic air transport, not all of the underlying multidisciplinary physics are thoroughly understood—yet very little work has been done in that direction on practical aircraft cases. This work builds upon the triglobal shock-buffet stability study by Timme [1] while aiming to investigate the impact of a flexible wing structure in these extreme flow conditions. The implementation of the coupled Jacobian matrix in an industrial solver enables the first triglobal stability analysis of a fluid-structure coupled system, utilising the implicitly restarted Arnoldi method with a sparse iterative Krylov solver and novel preconditioner. The chosen test case is the NASA Common Research Model for which both fluid modes on the rigid (yet statically deformed) wing and modes describing the dynamic aeroelastic behaviour (computed from a standard flutter analysis) guide the process. First, geometric asymmetry resulting from a static aeroelastic simulation based on a finite-element model of the wind-tunnel geometry modifies the global modes of the previous fluid-only symmetric full-span analysis. Second, flutter stability analysis at wind-tunnel flow conditions below shock-buffet onset finds no instability in the structural degrees of freedom, whereas in shock-buffet flow with globally unstable fluid modes additional marginally unstable structural (and fluid) modes are identified. Third, the coupled triglobal stability tool is indeed instrumental in identifying those physically dominant modes where a standard pk-type analysis fails. Together with our companion paper [2], we contribute to the question on how the presence of the flexible wing structure impacts on the otherwise pure aerodynamic three-dimensional shock-buffet dynamics.

Nomenclature

I	=	Identity matrix
J	=	Jacobian matrix
M, C, K	=	Mass, damping, stiffness matrices
m	=	Number of structural degrees of freedom
n_f	=	Number of fluid degrees of freedom
P	=	Preconditioner matrix
$\boldsymbol{R}$	=	Residual vector
S	=	Schur complement matrix
$\boldsymbol{w}$	=	State vector
$\boldsymbol{x}_s$	=	Structural vector
$\boldsymbol{\eta}$	=	Vector of generalised coordinates
$\lambda = \sigma + i\omega$	=	Eigenvalue with growth rate $\sigma = \mathrm{Re}(\lambda)$ and angular frequency $\omega = \mathrm{Im}(\lambda)$
Φ	=	Modal matrix from structural vibration analysis

*PhD Student, School of Engineering, jelle.houtman@liverpool.ac.uk.
†Senior Lecturer, School of Engineering, sebastian.timme@liverpool.ac.uk. Member AIAA.

I. Introduction

Aeroelasticity is the field of aerospace engineering that combines aerodynamic, elastic and inertial systems and was established over a century ago [3–5]. Since then, its study has clarified many important phenomena that plagued engineers and helped design countless aeroplanes, bridges, wind turbines and more. Static and dynamic instabilities such as divergence, violent flutter, limit-cycle oscillation and shock buffet (and its structural buffeting response) are detrimental to the safety, efficiency and comfort of an aeroplane and can even cause disastrous destruction. Therefore, the accurate and fast prediction of these phenomena is critical to inform aircraft design iterations. Major advances in numerical analysis of fluids and structures have offered invaluable insights in this process.

Shock buffet is a phenomenon whereby the interaction between a shock wave and a boundary layer results in strong, self-excited oscillations. While it has been known since the 1960s, a definite physical explanation incorporating all underlying multidisciplinary aspects still alludes researchers and design engineers alike. Since its discovery, experimental research has significantly increased its understanding and continues to this day [6–8]. One of the first explanations of shock buffet on aerofoils was given in [9], proposing an acoustic feedback loop that sustains the shock oscillations and several subsequent experimental studies supported the theoretical findings [7, 10]. For finite wings, on the other hand, spanwise outboard propagation of buffet cells has also been observed experimentally [8, 11] and numerically [12, 13]. The first numerical work to identify a global instability linked to aerofoil shock buffet was presented in [14, 15]. Since then, various studies have expanded on these findings, most recently by introducing generic infinite-wing geometries and investigating the impact of key geometric wing sizing parameters such as aspect ratio and sweep angle [16–18]. Practical finite-wing aircraft cases have also been studied by global stability analysis [1, 19, 20].

The mutual interaction between a flexible structure and shock buffet has been investigated previously, too. Importantly, it has been shown, for a pitch-plunge (and variants thereof) typical section aerofoil, that the introduction of an elastic structure has the ability to destabilise an otherwise stable flow [21]. That work also points out limitations of traditional flutter methods, such as a pk-type analysis, in tracing all relevant modes, prompting the development of more advanced methods. This is congruent with our discussion. The phenomenon of lock-in was found in different numerical studies. For instance, one degree-of-freedom pitch and two degree-of-freedom pitch-plunge typical section aerofoils were studied in [22] and the relation between the frequencies of the elastic structure and shock buffet was found critical in the analysis of lock-in and limit-cycle oscillations. Lock-in was also shown to be caused by fluid-mode flutter and not only as a resonance mechanism [23]. Experimental work on a finite wing found that weak shock-wave/boundary-layer interaction does not affect the structural system strongly, despite large flow field fluctuations [24]. With increasing shock strength due to higher free-stream Mach number, however, strong fluid-structure coupling was observed, despite weaker fluctuations in the flow overall, and the aeroelastic system responded to the unsteady flow excitation.

This contribution builds upon previous work in [1], that studied the fluid-only shock-buffet instability on a finite-wing aircraft. We introduce a coupled Jacobian matrix, accounting for the fluid-structure interaction, to enable the search for dominant fluid modes while at the same time determining the impact of the flexible wing structure. Previous work used the Schur complement method to trace aeroelastic modes describing the wing vibration [25, 26]. This formulation, which can be shown to be equivalent to legacy tools in industrial flutter analysis, is an efficient way of establishing the flutter boundary while making use of computational fluid dynamics functionality for the aerodynamics. However, it is unsuitable for finding fluid instabilities due to the mathematical structure of the coupled physics. The method introduced herein does not require any rearrangement or decomposition of the matrix eigenvalue problem. Our coupled solution approach with an inner-outer iterative structure relying on the shift-invert spectral transformation necessitated the implementation of a novel preconditioner for the inner sparse iterative linear equation solver, while offering speed-up compared to block-Jacobi type preconditioning. In previous work, the aerostructural coupled system has been solved in the context of adjoint gradient computation. Discipline-specific preconditioners from the fluid and structural solvers were reused in [27] in a block-Jacobi fashion, noting that discarding the off-diagonal coupling terms allows for easier parallelisation. Block-Jacobi and Gauss–Seidel preconditioners for a three-field formulation were compared in [28]. While this is an intricate discussion, clear performance gains were realised overall when including various coupling terms. A similar strategy of observing the discipline coupling is followed in our work.

This paper continues with a description of the physical models and implementation details in Section II. The focus is on the coupled Jacobian matrix and the adaptation of the iterative inner-outer eigenvalue solver, using the implicitly restarted Arnoldi method from the Arpack linear algebra library and a bespoke sparse iterative linear solver, all made available in the industrial DLR–TAU solver. The adoption of the Sherman–Morrison–Woodbury formula for the parallel inversion of block-arrowhead matrices in deriving a preconditioner for the coupled fluid-structure system and its benefits are discussed, too. As test case for method verification, the Goland wing is briefly considered. Results for the NASA Common Research Model are scrutinised in Section III.

II. Theory and Numerical Methods

A. Physical Models

The starting point of our work is the set of governing equations in semi-discrete form

$$\frac{\mathrm{d}\boldsymbol{w}}{\mathrm{d}t} = \boldsymbol{R}(\boldsymbol{w}), \tag{1}$$

where $\boldsymbol{w}$ is the state vector and $\boldsymbol{R}$ is the corresponding residual vector, which both comprise two parts, $\boldsymbol{w} = [\boldsymbol{w}_f^T, \boldsymbol{w}_s^T]^T$ and $\boldsymbol{R} = [\boldsymbol{R}_f^T, \boldsymbol{R}_s^T]^T$, representing the fluid and structure, respectively. In addition, the latter expression depends on a number of parameters which are not explicitly stated herein.

The fluid system is governed by the Reynolds-averaged Navier–Stokes (RANS) equations in three-dimensional space coupled with a suitable turbulence model. The fluid state vector $\boldsymbol{w}_f$ of conservative variables is given by $\boldsymbol{w}_f = [\rho, \rho\boldsymbol{u}, \rho E, \rho\tilde{\nu}]^T$, where ρ is the density, $\boldsymbol{u}$ the Cartesian velocity-field vector, E the energy and $\tilde{\nu}$ the working variable of the turbulence model, when using the negative Spalart–Allmaras model [29]. The governing equations written in integral form in the arbitrary Lagrangian Eulerian formulation can be stated as

$$\frac{\mathrm{d}}{\mathrm{d}t}\int_{\Omega(t)} \boldsymbol{w}_f \,\mathrm{d}V + \int_{\partial\Omega(t)} (\boldsymbol{F} - \boldsymbol{F}_v - \boldsymbol{w}_f \dot{\boldsymbol{x}}) \cdot \boldsymbol{n} \mathrm{d}S = \int_{\Omega(t)} \boldsymbol{Q} \mathrm{d}V, \tag{2}$$

where Ω is a time-dependent discrete control volume enclosed by $\partial\Omega$, the vectors $\boldsymbol{F}$ and $\boldsymbol{F}_v$ are the inviscid and viscous fluxes, respectively, $\boldsymbol{n}$ is the outward normal vector to $\partial\Omega$, $\dot{\boldsymbol{x}}$ is the mesh velocities vector and $\boldsymbol{Q}$ is the source term of the turbulence model. The discretised RANS equations (plus turbulence model) provide the fluid part of eq. (1) and $\boldsymbol{R}_f$ encompasses the last two integrals and an additional term arising from the discrete geometric conservation law. The dimension of the fluid system, n_f, is given by the number of mesh points times the number of conservative variables.

The structural system is governed by the second-order ordinary differential equation,

$$M\ddot{\boldsymbol{x}}_s + C\dot{\boldsymbol{x}}_s + K\boldsymbol{x}_s = \boldsymbol{f}, \tag{3}$$

where M, C and K represent the constant mass, damping and stiffness matrices, respectively, $\boldsymbol{f}$ are any present forces, specifically the aerodynamic forces in our case, and $\boldsymbol{x}_s$ are the structural coordinates. The deformation of the structure, $\boldsymbol{x}_s$, is given by $\boldsymbol{x}_s = \Phi\boldsymbol{\eta}$, where Φ is a matrix consisting of the spatial mode shapes of the structural system and $\boldsymbol{\eta}$ gives the temporal amplitude of each mode shape to the resulting deformation. Matrix Φ, together with the in-vacuum structural frequencies, is obtained from a vibration analysis of the underlying finite-element model. The structural equation of second-order is both projected into the modal space (using m dominant modes with lowest frequency) and rewritten as a first-order equation by standard augmentation, giving $\boldsymbol{w}_s = [\boldsymbol{\eta}^T, \dot{\boldsymbol{\eta}}^T]^T$ and $\boldsymbol{R}_s$ is the structural residual defined by

$$\boldsymbol{R}_s = D\boldsymbol{w}_s + \vartheta E\Phi^T \boldsymbol{f}(\boldsymbol{w}_f, \boldsymbol{w}_s), \tag{4}$$

where $D = [0, I; -\Phi^T K\Phi, -\Phi^T C\Phi]$ and $E = [0, I]^T$, with I being the $m \times m$ identity matrix. The mass ratio ϑ is the result of writing the equation in dimensionless form and is a function of reference density and length in our formulation. If the mode shapes are mass normalised such that the generalised mass matrix is $\Phi^T M\Phi = I$, the generalised stiffness matrix, $\Phi^T K\Phi$, is a diagonal matrix containing the squares of the angular frequencies of each mode. The dimension of the fluid problem, n_f, is much larger than that of the structural problem, $2m$, due to both the requirements on the resolution of the non-linear fluid flow and the linear nature of the structural model with constant mass, damping and stiffness matrices. We discard structural damping throughout in the following.

With the governing equations of the fluid and structural systems defined, we can return to eq. (1). Decomposing the unknown fluid and structural variables into steady-state base and perturbation vectors via $\boldsymbol{w}(t) = \bar{\boldsymbol{w}} + \tilde{\boldsymbol{w}}(t)$ results, after some more manipulation, in the linearised algebraic equations of the form

$$\frac{\mathrm{d}\tilde{\boldsymbol{w}}}{\mathrm{d}t} = J\tilde{\boldsymbol{w}} \tag{5}$$

where $J = \partial\boldsymbol{R}/\partial\boldsymbol{w}$ is the coupled Jacobian matrix, which is a large, sparse matrix consisting of four blocks $J = [J_{ff}, J_{fs}; J_{sf}, J_{ss}]$, with $J_{sf} = \vartheta E\Phi^T \partial\boldsymbol{f}/\partial\boldsymbol{w}_f$ and $J_{ss} = D + \vartheta E\Phi^T \partial\boldsymbol{f}/\partial\boldsymbol{w}_s$. If a solution ansatz of the form $\tilde{\boldsymbol{w}}(t) = \hat{\boldsymbol{w}}e^{\lambda t}$ is taken, eq. (5) can be recast as an eigenvalue problem,

$$\lambda\hat{\boldsymbol{w}} = J\hat{\boldsymbol{w}}, \tag{6}$$

where $\lambda = \sigma + i\omega$ denotes the eigenvalue, which is a complex number consisting of a growth rate σ and angular frequency ω, and $\hat{\boldsymbol{w}}$ is the corresponding eigenvector containing the complex amplitudes describing the coherent dynamics. When σ is greater than zero, the system is said to be globally unstable and this is what must be prevented within the aircraft flight envelope. Hence, the solution of this eigenvalue problem is desired as a first step in the analysis (once a non-linear equilibrium solution $\bar{\boldsymbol{w}}$ of eq. (1) is available).

B. Numerical Approach

Base State Calculation

The RANS equations (plus turbulence model) are solved using the industrial DLR–TAU code which uses a second-order, finite-volume, vertex-centred spatial discretisation [30]. The inviscid fluxes are computed using a central scheme with matrix artificial dissipation. The Green–Gauss theorem is used to evaluate the gradients of flow variables for viscous fluxes and source terms, where needed. Turbulence closure is provided by the negative Spalart–Allmaras model using the Boussinesq eddy-viscosity assumption. The far-field boundary is realised by the method of characteristics while the no-slip condition on viscous walls is enforced strongly. Additionally, when a symmetry plane boundary condition is required (specifically, for our wing test case to verify the implementation), this is imposed by removing components of the momentum equations normal to the plane. The steady-state flow solution is converged to low residual levels using the backward Euler method with lower-upper symmetric Gauss–Seidel iterations and local time-stepping. A geometric multi-grid method is also used to improve convergence rates.

The static aeroelastic solution of the coupled system is obtained by solving $\Phi^T K \Phi\, \boldsymbol{\eta} = \Phi^T \boldsymbol{f}(\boldsymbol{w}_f, \boldsymbol{\eta})$ iteratively, whereby the flow solver is integrated into the multidisciplinary simulation environment FlowSimulator, see for instance [31]. Note, since in the typical scenario the aerodynamic and structural points do not coincide, resulting in a coordinate mismatch between Φ and $\boldsymbol{f}$, the structural deformations have been splined to the aerodynamic surface mesh points, using radial basis function interpolation in a pre-processing step.

Aeroelastic Triglobal Stability Calculation

The Jacobian matrix blocks of the linearisation are calculated on the statically deformed geometry for subsequent stability analysis. Matrices J_{ff} and J_{sf} are computed from a hand-derived, analytical formulation, while J_{fs} is computed using a central finite-difference residual evaluation on the deformed volume mesh. Forming J_{ss} is trivial due to the modal nature of the structural system. Note that the viscous contribution to the aerodynamic forces $\boldsymbol{f}$ is discarded herein, leaving the pressure components only. Details on the meaning and simplifications can be found in [26], while a thorough discussion of the linear harmonic solver in DLR–TAU can be found in [32].

In previous work [26, 33, 34], the coupled fluid-structure system was solved using the Schur complement eigenvalue method. This method utilises the Schur complement matrix S to solve for the structural part of the eigenvalue problem in eq. (6). Rearranging gives

$$S(\lambda)\hat{\boldsymbol{w}}_s = \lambda \hat{\boldsymbol{w}}_s, \tag{7}$$

where $S(\lambda)$ is expressed as

$$S(\lambda) = J_{ss} - J_{sf}\,(J_{ff} - \lambda I)^{-1} J_{fs}, \tag{8}$$

and λ is an eigenvalue of the uncoupled structural system. This is an important condition, as will be seen below. The second part of the right-hand side of eq. (8) is dubbed the interaction matrix $Q = J_{sf}\,(J_{ff} - \lambda I)^{-1} J_{fs}$ and can be formed in both the frequency and time domain. It was noted by the authors that determining the values of the Schur complement matrix requires considerable computational effort, if not done effectively. As it depends on the steady-state solution and the eigenvalue, scanning over a large parameter space quickly becomes prohibitive, and thus approximations are needed. While multiple approaches to approximating matrix Q were offered, a linear spline interpolation was chosen as a surrogate herein while iterating to the eigensolution. Depending on using either λ or $i\omega$ in forming matrix Q, the Schur complement method can be shown to be equivalent to either a classical p or pk flutter analysis [35].

There are two requirements for the Schur complement method to work; an appropriate shift based on the structural (in-vacuum) frequencies (or a previously converged solution) and the matrix decomposition with relevant eigenmodes from J_{ss}. Whilst the former can be obtained through engineering insight even for a fluid mode, it is not possible to obtain the latter when interest is in modes emerging from the fluid system. Hence, a coupled eigenvalue solver is needed, incorporating the full Jacobian matrix. This can be done by using the methods available through the Arpack library.

Table 1 Typical parameter settings used for inner-outer eigenvalue solver.

Parameter	Value
Maximum number of eigenmodes per shift	5
Maximum number of outer iterations	1
Size of Krylov space for outer iterations	30
Convergence criterion on outer iterations	10^{-6}
Size of Krylov space for inner iterations	120
Number of deflation vectors for inner iterations	20
Convergence criterion on inner iterations	10^{-7}

The implicitly restarted Arnoldi method, as implemented in the Arpack library, is a routine for finding a set of eigenvalues for large sparse matrices [36]. Starting with a random vector $\boldsymbol{v}$, the algorithm computes, in principle, the so-called Krylov subspace, $\mathcal{K}_r = [\boldsymbol{v}, J\boldsymbol{v}, J^2\boldsymbol{v}, ..., J^{r-1}\boldsymbol{v}]$ of dimension r. After each multiplication with J, the resulting vector is orthonormalised and added as column to a matrix V_r. Following projection, a few Ritz eigenvalues λ_r and corresponding Ritz approximate eigenvectors $\hat{\boldsymbol{w}} = V_r \boldsymbol{y}_r$ (where eigenvector $\boldsymbol{y}_r$ is associated with λ_r) of the Hessenberg matrix $H_r = V_r^* J V_r$ are good approximations of those of J. A major advantage is that the algorithm needs only to compute the matrix-vector product $J\boldsymbol{v}$, so the full matrix J does not need to be stored explicitly. The algorithm can also be run in *shift-invert* mode to find the largest eigenvalues closest to a user-defined complex-valued shift ζ by operating on $\boldsymbol{v}$ with $(J - \zeta I)^{-1}$ instead of J. To achieve this, a linear system of the size of the coupled problem needs to be solved and a practical way is using an iterative Krylov subspace solver. An inner-outer iterative eigenvalue method is thus established, whereby the outer implicitly restarted Arnoldi process is used to find the eigenvalues while an inner iterative solver enables the shift-invert operation. The generalised conjugate residual method with deflated restarting (GCRO-DR) is used as the inner iterative solver [37]. Following the insight gained in [1], typical parameter settings for the eigenvalue computations discussed herein are summarised in table 1.

The GCRO-DR method is an iterative methods for solving systems of linear equations [38, 39]. It utilises the restarted Arnoldi method for solving the system $A\boldsymbol{x} = \boldsymbol{b}$ by seeking a solution vector $\boldsymbol{x}$ that minimises the norm of the residual $||\boldsymbol{b} - A\boldsymbol{x}||$. Specifically, compared with the standard generalized minimal residual method, GCRO-DR recycles the Krylov subspace between restarts, with the potential both to accelerate convergence and to reduce the required size of the subspace. A preconditioned version of Krylov subspace methods is needed in practice to achieve convergence, with the preconditioner P^{-1} being an approximation of A^{-1}. Ideally, P^{-1} should be as close to A^{-1} as possible, without incurring a large computational cost for both computing and applying the preconditioner. In doing so, using preconditioning reduces the condition number of the system and can offer significant speed-up.

When running the linear harmonic solver in DLR–TAU in parallel, the implementation approximates the fluid-only matrix used for preconditioning by a block-Jacobi form of J_{ff}. Specifically, when running on n cores, the Jacobian matrix J_{ff} would be split into n block-rows (one block-row per core including all entries needed for global matrix-vector products), and only the diagonal block of it is used for preconditioning. This matrix* is then factorised by the incomplete lower-upper method with 0 level of fill-in, denoted ILU(0). However, such approach poses a challenge for a fluid-structure coupled system in parallel, as the coupling matrices, J_{fs} and J_{sf}, would be discarded, when using an equivalent block-Jacobi formulation extended to the structural degrees-of-freedom. A new preconditioning approach, henceforth referred to as the arrowhead preconditioner, was used in the parallel implementation to address this coupling challenge. Initial testing was done with a simple case, specifically the coarse-mesh Goland wing described below, as the corresponding coupled Jacobian matrix was small enough to fit into memory of a single core and be factorised using ILU(0), without discarding the coupling blocks. The results from these sequential tests were then used as a benchmark to verify the implementation of the various code additions in parallel and assess the performance.

Arrowhead Preconditioner

When using the fully coupled Jacobian matrix in parallel, block-Jacobi preconditioning discards the coupling matrices, J_{sf} and J_{fs}. Therefore, incorporating these matrices in the formulation grants a better approximation of the

*Note that it was found beneficial for reasons of rate of convergence and stability to factorise a matrix which combines Jacobian matrices arising from approximate first-order and exact second-order spatial schemes [40].

Algorithm 1 Preprocessing stage for arrowhead preconditioner P^{-1}

Require: ILU decomposition of $J_{ff,i} \approx (LU)_i$, coupling matrices $J_{fs,i}$ and $J_{sf,i}$ (all local to each core i), and J_{ss}

1: Create $Y_i = (LU)_i^{-1} J_{fs,i}$ and store on respective core
2: Create $G_i = J_{sf,i}\, Y_i$ and sum globally to create $G = \sum_i G_i$ on each core
3: Create F by inverting $(J_{ss} - G)$ and store on each core ▷ done on each core, as F is only of size J_{ss}

Algorithm 2 Compute stage to obtain $P^{-1}\boldsymbol{v}$

Require: LU_i, Y_i, F, fluid vector $\boldsymbol{v}_{f,i}$ (local to each core i) and structural vector $\boldsymbol{v}_s$

1: Compute $\boldsymbol{w}_{f,i} = (LU)_i^{-1} \boldsymbol{v}_{f,i}$
2: Create $\boldsymbol{z}_i = J_{sf,i}\, \boldsymbol{w}_{f,i}$ and sum globally to obtain $\boldsymbol{z} = \sum_i \boldsymbol{z}_i$
3: Compute $\boldsymbol{w}_s = -F(\boldsymbol{z} - \boldsymbol{v}_s)$
4: Compute $\boldsymbol{w}_{f,i} = \boldsymbol{w}_{f,i} + Y_i\, \boldsymbol{w}_s$

inverse. This is possible by utilising an identity from a recent paper by Stanimirović et al. [41], which gives the inverse of a block-arrowhead matrix based on the Sherman–Morrison–Woodbury formula.

Block-arrowhead matrices have the form of

$$P = \begin{pmatrix} A_1 & 0 & 0 & \dots & B_1 \\ 0 & A_2 & 0 & \dots & B_2 \\ 0 & 0 & \ddots & & \vdots \\ \vdots & \vdots & & A_n & B_n \\ C_1 & C_2 & \dots & C_n & D \end{pmatrix}, \tag{9}$$

resembling our specific problem, where we define $A_i = J_{ff,i}$ (i.e. the local diagonal blocks of J_{ff}), $B_i = J_{fs,i}$, $C_i = J_{sf,i}$ and $D = J_{ss}$. Subscripts $i = 1, \dots, n$ denote the core number. Here, although all off-diagonal blocks of J_{ff} are discarded like before for the fluid-only problem, all elements of the other matrices are kept. The inverse of P is then given by

$$P^{-1} = \begin{pmatrix} A_1^{-1} & 0 & 0 & \dots & 0 \\ 0 & A_2^{-1} & 0 & \dots & 0 \\ 0 & 0 & \ddots & & \vdots \\ \vdots & \vdots & & A_n^{-1} & 0 \\ 0 & 0 & \dots & 0 & 0 \end{pmatrix} + \begin{pmatrix} A_1^{-1}B_1 \\ A_2^{-1}B_2 \\ \vdots \\ A_n^{-1}B_n \\ -I \end{pmatrix} \cdot F \cdot \begin{pmatrix} C_1A_1^{-1} & C_2A_2^{-1} & \dots & C_nA_n^{-1} & -I \end{pmatrix}, \tag{10}$$

where matrix F is define as

$$F = \left(D - \sum_{i=1}^{n} C_i\, A_i^{-1}\, B_i \right)^{-1}$$

and I is the identity matrix of the same dimensions as D. Computing the factor $A_i^{-1}\, B_i$ in F essentially requires applying the ILU factorisation of the fluid Jacobian matrix $J_{ff,i}$ to the $2m$ columns of matrix $J_{fs,i}$ (on each core locally). However, this needs to be done only once and for all, so computing $A_i^{-1}B_i$ and F can be done as a preprocessing step, described in algorithm 1. The additional memory requirements are one matrix of size J_{fs} and one of size J_{ss}. Preconditioning a random vector $\boldsymbol{v}$ is explained in algorithm 2. Compared to applying the block-Jacobi variant, besides operations on the negligible size of the structural system, only two additional matrix-vector products (one with matrix $J_{sf,i}$ and one with matrix Y_i), a vector-vector addition of size n_f and one global sum of size $2m$ are needed, which makes the computational overhead acceptable. Note, since matrix J_{sf} is very sparse with the only non-zero entries coming from the surface points where the generalised forces are integrated, matrix-vector products with this matrix are relatively cheap.

For debugging and verification purposes, the Goland wing was introduced. This wing is cantilevered with a constant 4%-thick, symmetric, parabolic-arc aerofoil and a span of 20 ft and chord of 6 ft. The structure is modelled by a

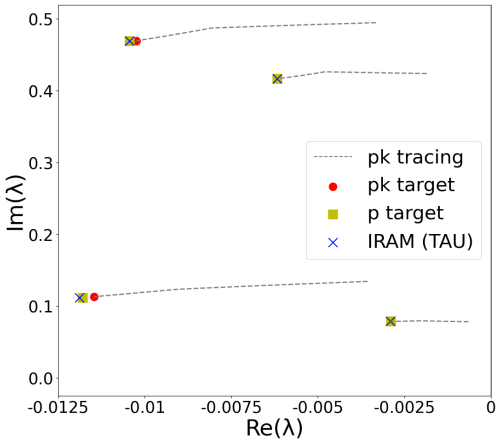

Fig. 1 Part of eigenspectrum for Goland wing test case (medium mesh) as computed by a pk-type method, showing trace with respect to altitude and eigenvalue at target altitude of 30 000 ft, compared with implicitly restarted Arnoldi method (IRAM) as implemented in DLR–TAU through coupling with Arpack library. An exact p-type analysis, without approximations on the linearised aerodynamic response, is also shown.

finite-element method (FEM), with details to be found in [42]. Two fluid meshes are used; one coarse mesh with approximately 20 000 points and one medium mesh with 400 000 points. Inviscid flow at a reference free-stream Mach number of $M = 0.845$ and zero degree angle of attack is assumed. The target altitude for the aeroelastic analysis is 30 000 ft. The steady-state solution for the Goland wing was computed using the Euler equations. To solve the eigenvalue problem in DLR–TAU, a maximum of 1 outer iteration was set with a Krylov space of 25 and a convergence criterion of 10^{-6}. The Krylov space for the inner iterations was 150 with 20 deflation vectors and a convergence criterion of 10^{-10}. This was done twice at shifts of $\zeta = 0.05 + 0.15i$ and $0.05 + 0.45i$, corresponding to the vicinity of the wind-off structural frequencies. Solely for debugging purposes, the relevant modes were first computed on the coarse mesh using three different methods, specifically the herein introduced coupled eigenvalue solver (running both sequential and parallel modes), the Schur complement method and a direct matrix solution using Matlab (which also makes use of the implicitly restarted Arnoldi eigenvalue method), after exporting the coupled matrix, and the agreement was excellent throughout. The same modes were computed on the medium mesh, using the Schur complement approach as both a pk- and p-type method, with details discussed in [25], as well as with our inner-outer iterative scheme through Arpack. Figure 1 shows the relevant part of the eigenspectrum. Indeed, the agreement of these different methods, specifically between the new coupled solver and the p-type analysis, indicates that the coupled eigenvalue solver has been implemented correctly, opening up the method to larger, more practical cases.

The speed-up gained by using the block-arrowhead preconditioner compared to the block-Jacobi preconditioner (easily implemented by setting all elements of the coupling blocks, J_{fs} and J_{fs}, in the preconditioner to zero) was insignificant for the inviscid Goland case without strong shock waves, whereas a 20% reduction in iteration count was observed from a limited number of trials for the significantly stiffer aircraft case in transonic turbulent flow (discussed in the next section), solving to an inner convergence tolerance of 10^{-7}.

III. Results and Discussion

The NASA Common Research Model (CRM) was designed to resemble a modern passenger aeroplane and exists both as physical (for wind-tunnel testing) and computational models. It was designed as a universal test case for researchers to compare new ideas and results [43]. The wing has an aspect ratio of 9, a taper ratio of 0.275 and a quarter-chord sweep angle of 35°. For this paper, the scaled-down wind-tunnel wing/body/horizontal-tail version was used with a mean aerodynamic chord of 0.189 m, a full span of 1.586 m and a reference area of 0.280 m^2. The pylons and nacelles were discarded and the tail-setting angle was 0°. The computational mesh was generated for the half-span simulations in [1] with the SOLAR mesh generator [44] and, upon mirroring with respect to the centre plane, the full-span case has approximately 12.3×10^6 mesh points with 3.3×10^5 points on solid walls. Additionally, the spherical far-field boundary is located 100 semi-span lengths away. The Reynolds number based on mean aerodynamic chord is $Re = 5.0 \times 10^6$ and the reference free-stream Mach number is $M = 0.85$, chosen based on runs 153/182 of the European

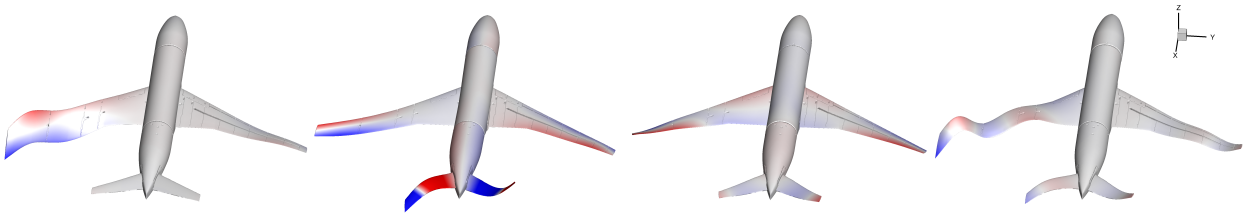

(a) Mode 20, 426.74 Hz **(b) Mode 27, 620.04 Hz** **(c) Mode 28, 641.54 Hz** **(d) Mode 29, 666.93 Hz**

Fig. 2 Representative structural mode shapes for NASA CRM test case with corresponding frequencies. Surface colours indicate the modal deformation in z-direction. Peculiar features on the aircraft surface are the various cut-outs on the wind-tunnel model for experimental sensors and to house the instrumentation.

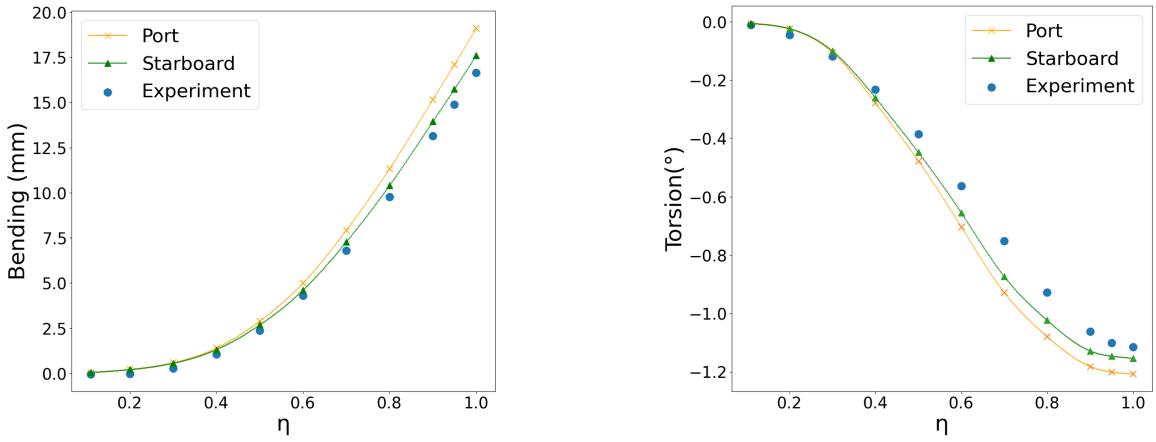

(a) Bending **(b) Wing twist**

Fig. 3 Bending and twist deformation over dimensionless span location η at $\alpha = 3.0°$ comparing experimental data from the ETW campaign and static aeroelastic results emphasising differences on port and starboard wing.

Transonic Windtunnel (ETW) test campaign [45]. The finite-element model represents the wind-tunnel geometry[†], and, following a modal structural analysis, the first 30 normal modes with lowest frequency are kept [46]. Importantly, the structural frequency range covers the shock-buffet frequency range previously identified. Figure 2 shows some of these modes, rescaled by a factor of 0.2 for visualisation purposes. The following results are stated in their non-dimensional form, based on the mean aerodynamic chord and reference free-stream values, unless explicitly specified otherwise.

Validation of Simulation Setup

The static aeroelastic solution of the aircraft model was computed at angle of attack $\alpha = 3.0°$ to match the loaded wind-tunnel shape and surface pressure data from run 182 in the ETW campaign. Figure 3 shows the bending and twist deformations on the port and starboard wing (evaluated at 50% chord) compared with those measured using stereo pattern tracking via markers distributed on the wing surface. Overall good agreement can be observed with a maximum bending of approximately 17 mm and a wash-out twist of $-1.1°$ at the wing tip. Importantly, an asymmetry between the port and starboard wing is also clearly visible in the numerical data. The cause of this asymmetry lies in the high fidelity of the finite-element model which takes into account the different cut-outs on each wing to house experimental sensors and related instrumentation. These features propagate to the normal mode shapes and their frequencies. For instance, the two first bending modes (one for port and one for starboard) have structural frequencies of 39.4 Hz and

[†]found at https://commonresearchmodel.larc.nasa.gov/

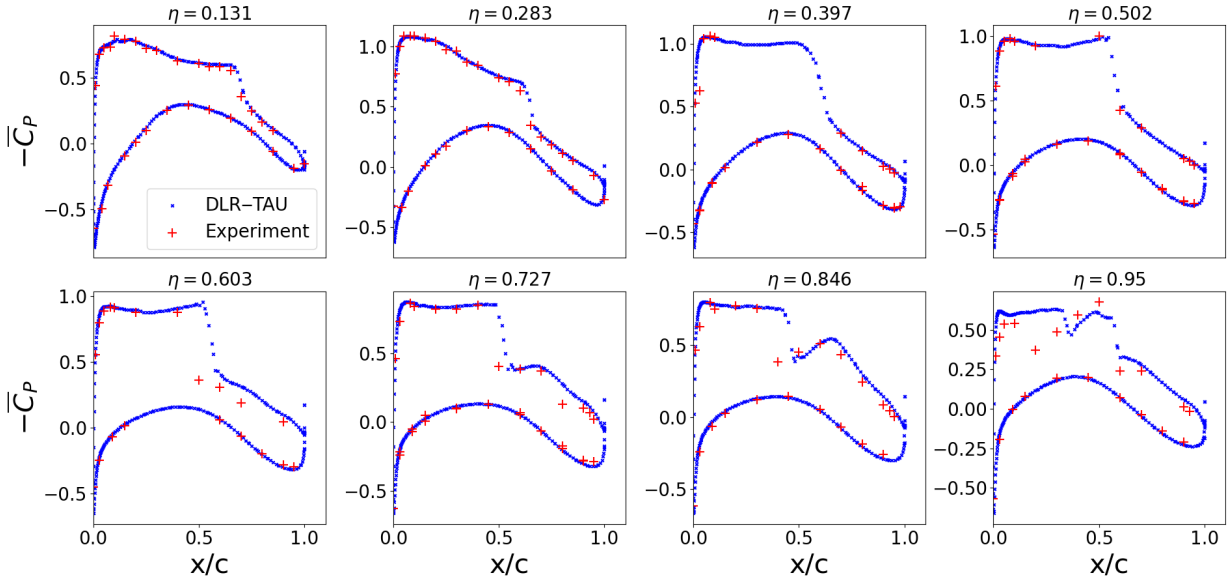

Fig. 4 Comparison of experimental and numerical surface pressure coefficient at angle of attack α = 3.0° at eight spanwise locations. Streamwise coordinate x is normalised by corresponding local chord length c.

40.9 Hz, respectively. The corresponding surface pressure coefficient of the steady base flow can be found in fig. 4 with good agreement to the experimental measurements at most spanwise stations. A discussion on the seemingly missing experimental data points around the mid semi-span was given in [1, 46]. Differences in the pressure coefficient between port and starboard wing are minor and not noticeable to the naked eye. A similar comparison at angle of attack $\alpha = 3.75°$, which is a key data point in our study and, importantly, used as coupled equilibrium solution (i.e. the steady base state) for all the subsequent analyses herein on the asymmetric geometry (*asymmetric* with respect to the fuselage centre plane), can be found in [2] and shows similar levels of agreement overall.

Flutter Analysis

Initially, eleven samples of the interaction matrix Q were computed using the linearised frequency-domain solver, assuming simple harmonic structural motion at reduced frequencies in the range $\omega = 0$ to 3 in increments of 0.3. The sampling frequency range corresponds to the wind-off structural frequencies, once made dimensionless based on the actual wind-tunnel flow conditions. This was done at two angles of attack $\alpha = 3.0°$ and 3.75°. Upon inspection of the results at the higher angle of attack, additional samples were added in regions of significant activity, bringing the total to 23. Figure 5 shows the absolute value of some selected entries of matrix Q. At the lower angle of attack, the matrix elements show a smooth trend with respect to the frequency. At the higher angle of attack, which describes a shock-buffet condition in the fluid-only analysis[‡], the entries have significant variation in the frequency range where the band of aerodynamic modes with increased growth rate is observed [1], specifically between approximately $\omega = 2.0$ and 3.0, indicating a strong coupling between the fluid and structure. The cause lies both in the proximity of the sampling frequency to some eigenvalues of the coupled system and in the non-normality of the governing equations [47]. For instance, the significant peaks at a forcing frequency of approximately $\omega = 2.7$ coincide with one computed eigenvalue, labelled c', of the band of shock-buffet modes shown in fig. 7 below.

Figure 6 shows the predicted eigenvalues from the flutter analysis at angles of attack $\alpha = 3.0°$ and 3.75° at the target flow condition encountered in the wind-tunnel environment. Since tracing the eigenmodes is somewhat arbitrary and would depend on how the test point is reached in the wind tunnel, we chose to increase the density until the simulated flow condition matches the experiment, while keeping all other variables, specifically velocity, temperature and pressure, frozen. The target corresponds to a density of 1.53 kg m^{-3}. The eigenvalues at $\alpha = 3.0°$ show no instabilities, indicating the system is stable. At $\alpha = 3.75°$, it is visible that modes with frequencies below approximately $\omega = 1.7$ have changed very little compared with the lower angle of attack. At the same time, instabilities are found for structural modes 19, 20,

[‡]Interpreting a linearised frequency-domain aerodynamic response to a structural forcing in globally unstable flow should be done carefully.

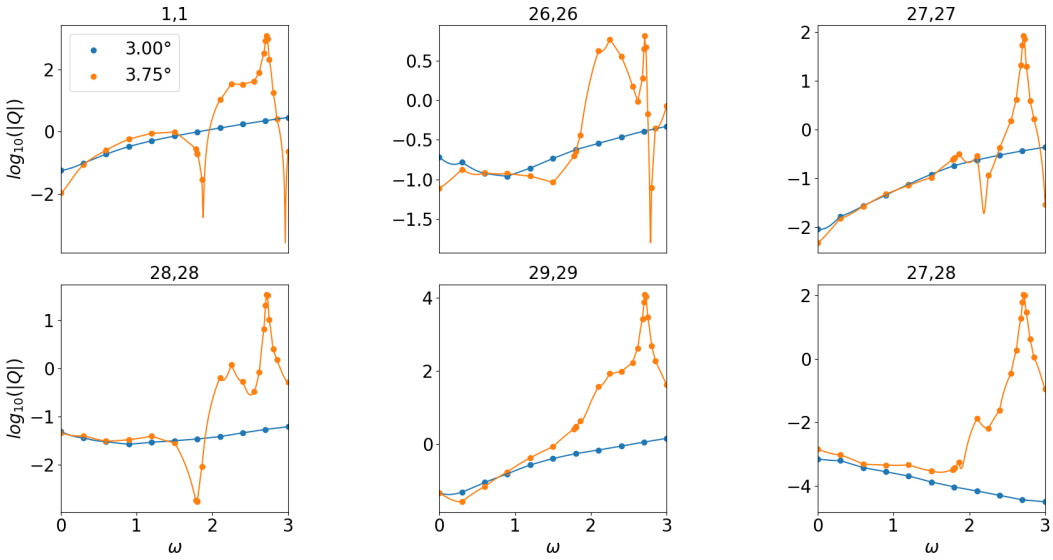

Fig. 5 Magnitude of complex values for various entries of matrix Q at $\alpha = 3.0°$ and $3.75°$ in log-scale, along with the linear spline interpolation used for mode tracing, over sampling frequency ω.

21 and 27. Mode 28 (denoted •), starting at a frequency of 2.72, did not trace correctly and instead jumped onto a different mode, despite the additional samples around this frequency to avoid heavy reliance on interpolation. This was attributed to the fact that the interaction matrix Q, and therefore $S(\lambda)$ in eq. (8), shows extreme variation due to the shifted matrix $(J_{ff} - \lambda I)$ being close to singular. This provides another reason for the use of the coupled Arpack method, besides the ability to compute fluid modes in the first place, as it can distinguish between fluid and structural modes in highly contested regions. It has been noted that the second term of matrix $J_{ss} = D + \vartheta E \Phi^T \partial \boldsymbol{f} / \partial \boldsymbol{w}_s$ can often be discarded [34]. This was confirmed herein for the CRM test case by evaluating the sensitivity of the generalised forces with respect to the modal amplitudes (at fixed flow solution). The added term had negligible influence on the results. Viscous force contributions were also discarded for similar reasons.

Aerodynamic Global Stability Analysis

We are now interested in elucidating the impact of the asymmetrically deformed full-span wing geometry on the aerodynamic stability characteristics at angle of attack $\alpha = 3.75°$. For the eigenspectra computed by Arpack, multiple shifts were used to cover the relevant frequency range. Figure 7 shows the eigenspectra of the fluid-only system on the left, as computed on the perfectly symmetric case (*symmetric* with respect to the fuselage centre plane) and the asymmetric case from our static aeroelastic simulation, cf. the deformation presented in fig. 3. The full-span symmetric data are taken from [1] and the labelling follows accordingly. While the symmetric, pre-deformed geometry (corresponding to deformations measured in run 182 of the experimental campaign) gives two nearly identical unstable eigenvalues at approximately $\lambda = 0.16 + 2.37i$, the asymmetric geometry from the static coupling simulation results in two visibly distinct eigenvalues. In the symmetric case, the corresponding eigenvectors revealed symmetric/anti-symmetric coherent spatial structures of equal amplitudes on both wings. Interestingly, for the asymmetric, statically deformed geometry, on the other hand, the coherent spatial structures of the two unstable modes, while appearing similar to the coherent features on the symmetric geometry, now dominate one wing each, as presented in fig. 8. The figure shows the magnitude of the unsteady surface pressure coefficient of the two unstable global shock-buffet modes, labelled *b* in fig. 7, and a visualisation of coherent structures through the volumetric iso-surfaces of the real part of the x-momentum $\widehat{\rho u}$ at values of ±0.01. Note that the mode with the highest growth rate shows activity on the port wing. Another mode, labelled *c'*, migrated significantly, approaching the unstable region, and we will return to discussing this mode shortly.

Coupled Aeroelastic Global Stability Analysis

The ramification of including a flexible aircraft structure in the stability analysis is now elucidated. Figure 7 on the right gives the eigenspectra as computed by Arpack for the fluid-only system, labelled *asym. (fluid-only)*, and for

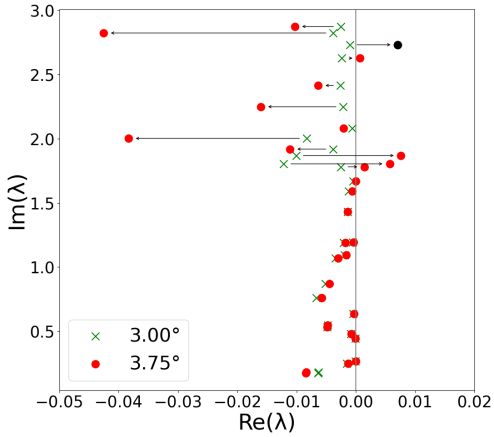

Fig. 6 Eigenvalues from flutter analysis at $\alpha = 3.0°$ and $3.75°$ at the flow condition encountered in the wind-tunnel environment. Mode 28 at $\alpha = 3.75°$, denoted •, failed to converge.

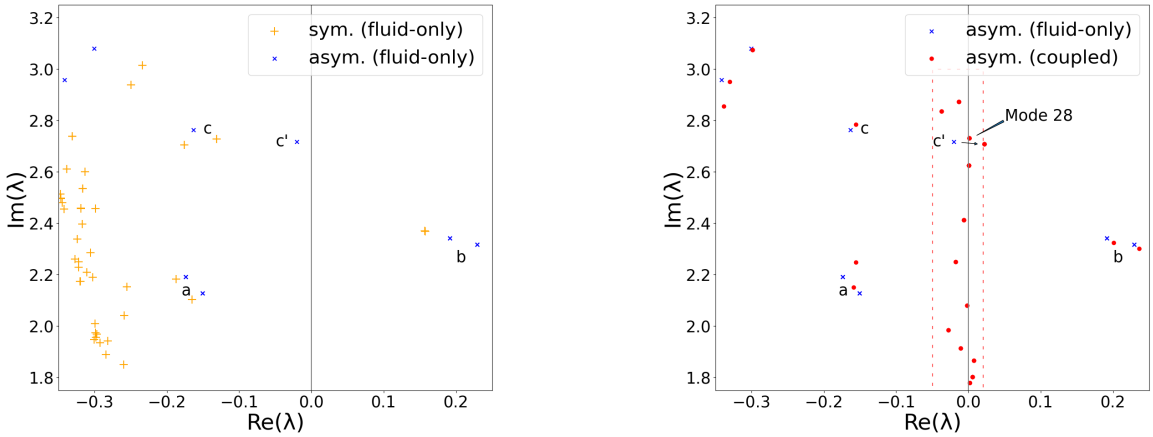

Fig. 7 Comparison of eigenspectra showing (left) fluid-only results for symmetric versus asymmetric geometry and (right) asymmetric fluid-only versus coupled results. Modes are labelled according to [1], along with mode c', which migrates into the unstable region in the coupled system. All unannotated coupled modes in the right plot are structural modes. Note the red box indicating the relevant region from fig. 6 for reference.

the coupled system, labelled *asym. (coupled)*. All structural modes found with the pk-type flutter analysis (bar the aforementioned difficulties with mode 28) were also found by the Arpack eigenvalue analysis of the coupled system, further supporting the notion that the implementation is working correctly. Multiple interesting features can be observed. The discussion focuses on three regions of the eigenspectrum, specifically the leading shock-buffet modes b, the unstable structural modes around $\omega = 1.8$, and the unstable modes 27, 28 and c' at approximately $\omega = 2.7$.

First, the two unstable shock-buffet modes, denoted b, are also observed in the coupled system, albeit at slightly decreased frequencies and increased growth rates. This suggests that including a flexible structure could destabilise an otherwise stable fluid-only mode at a reduced angle of attack. These shock-buffet modes again emphasise a separate wing each, as pictured in fig. 9, and the surface flow characteristics (not included in the plot for reasons of clarity) are very similar to their fluid-only counterparts in fig. 8. An interpretation could be that the shock-buffet unsteadiness remains the dominant physics even when including the flexible wing structure. Having said this, the structural part of the eigenvectors shows highest activity (i.e. deformation) on the same wing as the coherent spatial flow features, revealing a coupling effect. To be clear, magnitude of wing deformation is visualised through the relation $|\hat{\boldsymbol{x}}_s| = \boldsymbol{\Phi}|\hat{\boldsymbol{\eta}}|$.

Second, for the group of eigenvalues around $\omega = 1.8$, the Arpack method does indeed identify three unstable structural modes, specifically modes 19, 20 and 21, also found by the earlier flutter analysis. The coherent flow features of these modes' eigenvectors (not explicitly shown herein for reasons of brevity) closely resemble those of the shock-buffet

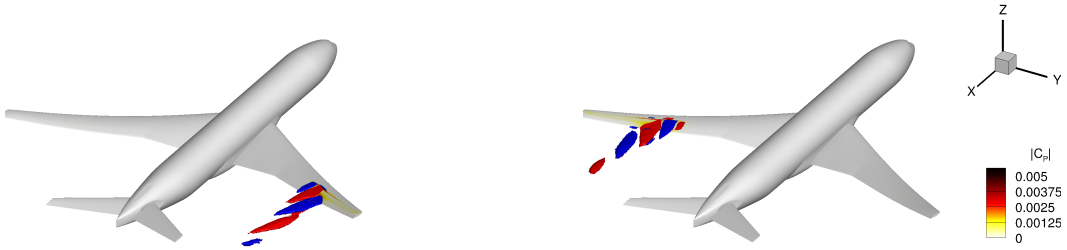

Fig. 8 Magnitude of unsteady surface pressure coefficient $|\hat{C}_p|$ and volumetric iso-surfaces of real part of x-momentum $\widehat{\rho u}$ at values of ±0.01 of the two unstable global modes from fluid-only stability analysis on statically deformed, asymmetric geometry. Underlying eigenvectors are unit length.

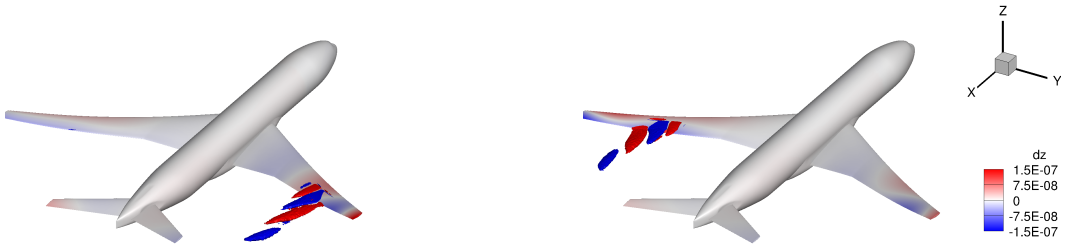

Fig. 9 Visualisation of unstable shock-buffet modes of fluid-structure coupled system (labelled *b* in fig. 7). Surface contours show magnitude of unsteady deformation in z-direction derived from structural part $\hat{\boldsymbol{\eta}}$ of coupled eigenvector, while volumetric iso-surfaces illustrate real part of x-momentum $\widehat{\rho u}$ at values of ±0.01. Underlying eigenvectors are unit length. A strong resemblance to the fluid-only modes in fig. 8 can be observed.

modes *b*. Having said this, a correlation between the frequencies of coherent modes and their spatial amplitudes was observed in [1], which is also seen in the coherent flow features of the structural modes. The spanwise wavelengths are larger than those of the shock-buffet modes *b*, in accordance with their lower frequencies. Furthermore, the largest entries in the structural part $\hat{\boldsymbol{\eta}}$ of their unit-length eigenvectors correspond to position 19, 20 and 21, respectively, by at least an order of magnitude higher amplitude compared to the other entries. Consequently, the structural motion described by these coupled modes is rather similar to that of their respective wind-off structural mode shapes.

Third, from the group of eigenvalues around $\omega = 2.7$, the structural mode labelled *Mode 28* in fig. 7, which the pk-type Schur complement method was unable to trace, is now identified to be unstable. The coherent flow features of eigenmodes 27 and 28 are similar to one of the shock-buffet modes *b* emphasising the port wing, but have smaller spanwise wavelengths, as is expected from their higher frequencies. Their frequencies are close to the wind-off structural frequencies of modes 27 and 28, and the largest entry, by an order of magnitude, in their respective vector $\hat{\boldsymbol{\eta}}$ again agrees with the mode number. Consequently, comparing fig. 2 with fig. 10, the wing deformations are similar. As this is also the case for the second group of interesting (unstable) modes around $\omega = 1.8$, it is reasonable to conclude that *Mode 28* originated in the structural system, even though the pk flutter method failed in tracing it. Also, the one remaining unstable mode at $\lambda = 0.02 + 2.71i$ did not originate in the structure, but is indeed mode c', originating in the fluid system, which migrated into the unstable half-plane due to strong fluid-structure interaction. The coupled mode c' has coherent flow features around the port wing, shown in fig. 10, and these are very similar to those of its fluid-only counterpart (not shown herein). Its corresponding vector $\hat{\boldsymbol{\eta}}$ has a largest entry 28, with entries 27 and 29 following closely. This is further evidence that it is unlikely a structural mode. Besides our earlier statement that the coupling of aerodynamics with a flexible wing structure can destabilise the global flow field earlier, a second finding in this regard is the ability to destabilise additional, otherwise stable, fluid-only modes. For further insight into these unstable structural modes, consult our companion paper which discusses unsteady time-marching fluid-structure coupled simulations on the same geometry while focussing both on the initial growth of disturbances and the non-linear saturation [2].

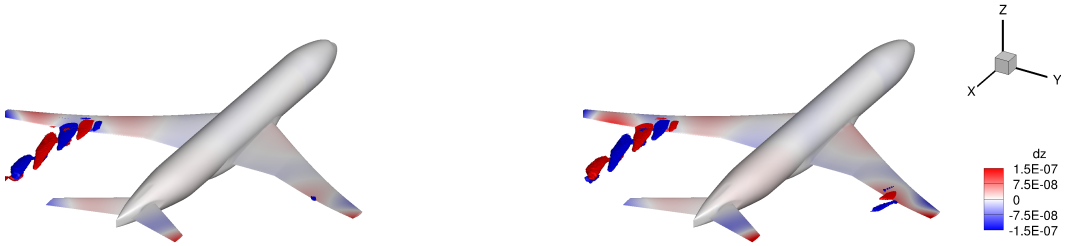

Fig. 10 Visualisation of unstable mode c' (left) and structural mode 28 (right) of the coupled system. Chosen variables and styles are identical to those in fig. 9.

IV. Conclusion

To investigate the mutual interaction between a flexible wing structure and the shock-buffet phenomenon (which is self-sustained even without wing vibration), the linear harmonic incarnation of the industrial DLR–TAU solver was successfully modified to implement a fluid-structure coupled system enabling its global mode computation using the shift-invert implicitly restarted Arnoldi method as outer iteration together with an inner sparse iterative linear equation solver. Preconditioning the inner Krylov iterative method using a novel approach based on a so-called block-arrowhead matrix offers speed-up gains in parallel computation needed for a stiff practical aircraft case in transonic turbulent flow. The new code additions permit the first computation of dominant fluid modes together with modes originating in the structural system, even in close frequency proximity, when a conventional pk-type flutter analysis can fail.

The chosen test case is the NASA Common Research Model with limited experimental data from a European Transonic Windtunnel test campaign. Static aeroelastic deformations together with the steady base flow at two angles of attack show good agreement with wind-tunnel data, and those results are used as equilibrium solution for the subsequent linearised analyses. Importantly, an asymmetric wing deformation (with respect to the fuselage centre plane), as a consequence of using a finite-element structural model of the actual wind-tunnel geometry, is observed, resulting in pairs of global modes with each mode of a pair emphasising a different wing. This is in stark contrast to a previous stability study on a perfectly symmetric full-span geometry giving pairs of symmetric/anti-symmetric global modes. For routine flutter analyses, aerodynamic influence matrices were computed with the linear harmonic solver following modal structural excitation. Despite the large number of samples in the shock-buffet frequency range, the pk flutter method was unable to trace all structural modes unambiguously, owing to a strong interaction between fluid and structure. Finally, the coupled global mode approach succeeded in correctly identifying all structural modes as well as the previously found fluid modes. Most interestingly, several unstable structural modes appear in the shock-buffet frequency range in addition to yet another unstable mode linked to the fluid. This mode is stable in the fluid-only system, indicating the inclusion of a flexible structure could see previously stable modes become unstable. Its coherent spatial characteristics from the eigenvector are similar to those of its fluid-only counterpart, whilst the structural part is strongly influenced by the surrounding structural modes close to that frequency. This suggests that fluid-structure interaction should not be discarded when investigating shock-buffet and buffeting phenomena.

Acknowledgments

The first author is grateful for the financial support by an Engineering and Physical Sciences Research Council (EPSRC) Industrial CASE scholarship in partnership with Airbus. We also thank the University of Liverpool for computing time on the high-performance computer.

References

[1] Timme, S., "Global instability of wing shock-buffet onset," *Journal of Fluid Mechanics*, Vol. 885, 2020, p. A37. https://doi.org/10.1017/jfm.2019.1001.

[2] Belesiotis-Kataras, P., and Timme, S., "Aeroelastic Coupling Effects in Globally Unstable Transonic Wing Flow," *AIAA SciTech 2021 Forum*, 2021.

[3] Livne, E., "Future of Airplane Aeroelasticity," *Journal of Aircraft*, Vol. 40, No. 6, 2003, pp. 1066–1092. https://doi.org/10.2514/2.7218.

[4] Shubov, M. A., "Flutter Phenomenon in Aeroelasticity and Its Mathematical Analysis," *Journal of Aerospace Engineering*, Vol. 19, No. 1, 2006, pp. 1–12. https://doi.org/10.1061/(ASCE)0893-1321(2006)19:1(1).

[5] Beran, P., Stanford, B., and Schrock, C., "Uncertainty Quantification in Aeroelasticity," *Annual Review of Fluid Mechanics*, Vol. 49, No. 1, 2017, pp. 361–386. https://doi.org/10.1146/annurev-fluid-122414-034441.

[6] Tijdeman, H., "Investigations of the transonic flow around oscillating airfoils," Tech. Rep. NLR-TR 77090 U, Nationaal Lucht-en Ruimtevaartlaboratorium, 1977. URL http://resolver.tudelft.nl/uuid:b07421b9-136d-494c-a161-b188e5ba1d0d.

[7] Jacquin, L., Molton, P., Deck, S., Maury, B., and Soulevant, D., "Experimental Study of Shock Oscillation over a Transonic Supercritical Profile," *AIAA Journal*, Vol. 47, No. 9, 2009, pp. 1985–1994. https://doi.org/10.2514/1.30190.

[8] Dandois, J., "Experimental study of transonic buffet phenomenon on a 3D swept wing," *Physics of Fluids*, Vol. 28, No. 1, 2016, 016101. https://doi.org/10.1063/1.4937426.

[9] Lee, B. H. K., "Oscillatory shock motion caused by transonic shock boundary-layer interaction," *AIAA Journal*, Vol. 28, No. 5, 1990, pp. 942–944. https://doi.org/10.2514/3.25144.

[10] Feldhusen-Hoffmann, A., Statnikov, V., Klaas, M., and Schröder, W., "Investigation of shock-acoustic-wave interaction in transonic flow," *Experiments in Fluids*, Vol. 59, No. 1, 2018, 15. https://doi.org/10.1007/s00348-017-2466-z.

[11] Masini, L., Timme, S., and Peace, A. J., "Analysis of a civil aircraft wing transonic shock buffet experiment," *Journal of Fluid Mechanics*, Vol. 884, 2020, p. A1. https://doi.org/10.1017/jfm.2019.906.

[12] Sartor, F., and Timme, S., "Delayed Detached–Eddy Simulation of Shock Buffet on Half Wing–Body Configuration," *AIAA Journal*, Vol. 55, No. 4, 2017, pp. 1230–1240. https://doi.org/10.2514/1.J055186.

[13] Ohmichi, Y., Ishida, T., and Hashimoto, A., "Modal Decomposition Analysis of Three-Dimensional Transonic Buffet Phenomenon on a Swept Wing," *AIAA Journal*, Vol. 56, No. 10, 2018, pp. 3938–3950. https://doi.org/10.2514/1.J056855.

[14] Crouch, J., Garbaruk, A., and Magidov, D., "Predicting the onset of flow unsteadiness based on global instability," *Journal of Computational Physics*, Vol. 224, No. 2, 2007, pp. 924 – 940. https://doi.org/10.1016/j.jcp.2006.10.035.

[15] Crouch, J. D., Garbaruk, A., Magidov, D., and Travin, A., "Origin of transonic buffet on aerofoils," *Journal of Fluid Mechanics*, Vol. 628, 2009, p. 357–369. https://doi.org/10.1017/S0022112009006673.

[16] Paladini, E., Beneddine, S., Dandois, J., Sipp, D., and Robinet, J.-C., "Transonic buffet instability: From two-dimensional airfoils to three-dimensional swept wings," *Physical Review Fluids*, Vol. 4, 2019, p. 103906. https://doi.org/10.1103/PhysRevFluids.4.103906.

[17] Crouch, J. D., Garbaruk, A., and Strelets, M., "Global instability in the onset of transonic-wing buffet," *Journal of Fluid Mechanics*, Vol. 881, 2019, p. 3–22. https://doi.org/10.1017/jfm.2019.748.

[18] He, W., and Timme, S., "Triglobal Shock Buffet Instability Study on Infinite Wings," *AIAA SciTech 2020 Forum*, 2020. https://doi.org/10.2514/6.2020-1986, AIAA 2020-1986.

[19] Timme, S., and Thormann, R., "Towards three-dimensional global stability analysis of transonic shock buffet," *AIAA Atmospheric Flight Mechanics Conference*, 2016. https://doi.org/10.2514/6.2016-3848, AIAA 2016-3848.

[20] Timme, S., "Global Shock Buffet Instability on NASA Common Research Model," *AIAA SciTech 2019 Forum*, 2019. https://doi.org/10.2514/6.2019-0037, AIAA 2020-0037.

[21] Nitzsche, J., Ringel, L. M., Kaiser, C., and Hennings, H., "Fluid-mode flutter in plane transonic flows," *IFASD 2019 – International Forum on Aeroelasticity and Structural Dynamics*, 2019. URL https://elib.dlr.de/127989/.

[22] Raveh, D. E., and Dowell, E. H., "Aeroelastic Responses of Elastically Suspended Airfoil Systems in Transonic Buffeting Flows," *AIAA Journal*, Vol. 52, No. 5, 2014, pp. 926–934. https://doi.org/10.2514/1.J052185.

[23] Gao, C., Zhang, W., Li, X., Liu, Y., Quan, J., Ye, Z., and Jiang, Y., "Mechanism of frequency lock-in in transonic buffeting flow," *Journal of Fluid Mechanics*, Vol. 818, 2017, p. 528–561. https://doi.org/10.1017/jfm.2017.120.

[24] Steimle, P. C., Karhoff, D.-C., and Schröder, W., "Unsteady Transonic Flow over a Transport-Type Swept Wing," *AIAA Journal*, Vol. 50, No. 2, 2012, pp. 399–415. https://doi.org/10.2514/1.J051187.

[25] Bekemeyer, P., and Timme, S., "Flexible aircraft gust encounter simulation using subspace projection model reduction," *Aerospace Science and Technology*, Vol. 86, 2019, pp. 805 – 817. https://doi.org/10.1016/j.ast.2019.02.011.

[26] Badcock, K., Timme, S., Marques, S., Khodaparast, H., Prandina, M., Mottershead, J., Swift, A., Ronch], A. D., and Woodgate, M., "Transonic aeroelastic simulation for instability searches and uncertainty analysis," *Progress in Aerospace Sciences*, Vol. 47, No. 5, 2011, pp. 392 – 423. https://doi.org/10.1016/j.paerosci.2011.05.002.

[27] Kenway, G. K. W., Kennedy, G. J., and Martins, J. R. R. A., "Scalable Parallel Approach for High-Fidelity Steady-State Aeroelastic Analysis and Adjoint Derivative Computations," *AIAA Journal*, Vol. 52, No. 5, 2014, pp. 935–951. https://doi.org/10.2514/1.J052255.

[28] Zhang, Z. J., and Zingg, D. W., "Efficient Monolithic Solution Algorithm for High-Fidelity Aerostructural Analysis and Optimization," *AIAA Journal*, Vol. 56, No. 3, 2018, pp. 1251–1265. https://doi.org/10.2514/1.J056163.

[29] Allmaras, S., Johnson, F., and Spalart, P., "Modifications and clarifications for the implementation of the Spalart-Allmaras turbulence model," *Seventh International Conference on Computational Fluid Dynamics (ICCFD7)*, 2012, pp. 1–11.

[30] Schwamborn, D., Gerhold, T., and Heinrich, R., "The DLR TAU-code: Recent applications in research and industry," *ECCOMAS CFD 2006: Proceedings of the European Conference on Computational Fluid Dynamics*, 2006.

[31] Reimer, L., Heinrich, R., and Ritter, M., "Towards Higher-Precision Maneuver and Gust Loads Computations of Aircraft: Status of Related Features in the CFD-Based Multidisciplinary Simulation Environment FlowSimulator," *New Results in Numerical and Experimental Fluid Mechanics XII*, edited by A. Dillmann, G. Heller, E. Krämer, C. Wagner, C. Tropea, and S. Jakirlić, Springer International Publishing, Cham, 2020, pp. 597–607. https://doi.org/10.1007/978-3-030-25253-3_57.

[32] Thormann, R., and Widhalm, M., "Linear-Frequency-Domain Predictions of Dynamic-Response Data for Viscous Transonic Flows," *AIAA Journal*, Vol. 51, No. 11, 2013, pp. 2540–2557. https://doi.org/10.2514/1.J051896.

[33] Timme, S., and Badcock, K. J., "Transonic Aeroelastic Instability Searches Using Sampling and Aerodynamic Model Hierarchy," *AIAA Journal*, Vol. 49, No. 6, 2011, pp. 1191–1201. https://doi.org/10.2514/1.J050509.

[34] Timme, S., Marques, S., and Badcock, K. J., "Transonic Aeroelastic Stability Analysis Using a Kriging-Based Schur Complement Formulation," *AIAA Journal*, Vol. 49, No. 6, 2011, pp. 1202–1213. https://doi.org/10.2514/1.J050975.

[35] Hassig, H. J., "An approximate true damping solution of the flutter equation by determinant iteration," *Journal of Aircraft*, Vol. 8, No. 11, 1971, pp. 885–889. https://doi.org/10.2514/3.44311.

[36] Sorensen, D. C., "Implicit Application of Polynomial Filters in a k-Step Arnoldi Method," *SIAM Journal on Matrix Analysis and Applications*, Vol. 13, No. 1, 1992, pp. 357–385. https://doi.org/10.1137/0613025.

[37] Xu, S., and Timme, S., "Robust and efficient adjoint solver for complex flow conditions," *Computers & Fluids*, Vol. 148, 2017, pp. 26 – 38. https://doi.org/10.1016/j.compfluid.2017.02.012.

[38] Parks, M. L., de Sturler, E., Mackey, G., Johnson, D. D., and Maiti, S., "Recycling Krylov Subspaces for Sequences of Linear Systems," *SIAM Journal on Scientific Computing*, Vol. 28, No. 5, 2006, pp. 1651–1674. https://doi.org/10.1137/040607277.

[39] Eiermann, M., Ernst, O. G., and Schneider, O., "Analysis of acceleration strategies for restarted minimal residual methods," *Journal of Computational and Applied Mathematics*, Vol. 123, No. 1, 2000, pp. 261 – 292. https://doi.org/10.1016/S0377-0427(00)00398-8, numerical Analysis 2000. Vol. III: Linear Algebra.

[40] McCracken, A., Ronch, A. D., Timme, S., and Badcock, K., "Solution of linear systems in Fourier-based methods for aircraft applications," *International Journal of Computational Fluid Dynamics*, Vol. 27, No. 2, 2013, pp. 79–87. https://doi.org/10.1080/10618562.2012.750719.

[41] Stanimirović, P. S., Katsikis, V. N., and Kolundžija, D., "Inversion and pseudoinversion of block arrowhead matrices," *Applied Mathematics and Computation*, Vol. 341, 2019, pp. 379 – 401. https://doi.org/10.1016/j.amc.2018.09.006.

[42] Beran, P. S., Khot, N. S., Eastep, F. E., Snyder, R. D., and Zweber, J. V., "Numerical Analysis of Store-Induced Limit-Cycle Oscillation," *Journal of Aircraft*, Vol. 41, No. 6, 2004, pp. 1315–1326. https://doi.org/10.2514/1.404.

[43] Vassberg, J., Dehaan, M., Rivers, M., and Wahls, R., "Development of a Common Research Model for Applied CFD Validation Studies," *26th AIAA Applied Aerodynamics Conference*, 2008. https://doi.org/10.2514/6.2008-6919.

[44] Martineau, D., Stokes, S., Munday, S., Jackson, A., Gribben, B., and Verhoeven, N., *Anisotropic Hybrid Mesh Generation for Industrial RANS Applications*, chapter and pages. https://doi.org/10.2514/6.2006-534.

[45] Lutz, T., Gansel, P. P., Waldmann, A., Zimmermann, D.-M., and Schulte am Hülse, S., "Prediction and Measurement of the Common Research Model Wake at Stall Conditions," *Journal of Aircraft*, Vol. 53, No. 2, 2016, pp. 501–514. https://doi.org/10.2514/1.C033351.

[46] Tinoco, E. N., Brodersen, O. P., Keye, S., Laflin, K. R., Feltrop, E., Vassberg, J. C., Mani, M., Rider, B., Wahls, R. A., Morrison, J. H., Hue, D., Roy, C. J., Mavriplis, D. J., and Murayama, M., "Summary Data from the Sixth AIAA CFD Drag Prediction Workshop: CRM Cases," *Journal of Aircraft*, Vol. 55, No. 4, 2018, pp. 1352–1379. https://doi.org/10.2514/1.C034409.

[47] He, W., and Timme, S., "Resolvent Analysis of Shock Buffet on Infinite Wings," *AIAA Aviation 2020 Forum*, 2020. https://doi.org/10.2514/6.2020-2727, AIAA 2020-2727.